(Received 9 November 2025, Accepted 20 November 2025, Scheduled 19 December 2025)

Design of Near-field Focusing Optical Transparent Metasurface for Millimeter-wave Communication

Licong Fan[1], Yuan Yao[2], Jingchang Nan[1,*], and Yifei Wang[1]

[1]*School of Electronics and Information Engineering, Liaoning University of Engineering and Technology, Huludao, China*
[2]*School of Electronics Engineering, Beijing University of Posts and Telecommunications, Beijing, China*

ABSTRACT: Low-emissivity glass, commonly employed in building curtain walls, strongly reflects and weakly transmits millimeter-wave signals, thereby hindering signal propagation. To address this issue, this paper introduces a novel method that leverages the low-emissivity film itself to design a metasurface for enhanced signal transmission. Two specific metasurface designs are presented. The simulation results validate the proposed method. For the design targeting linearly polarized waves, a 23 dB enhancement in the transmitted electric field is achieved compared to that of uncoated glass. The design for circularly polarized waves achieves a 22 dB enhancement. Both metasurfaces exhibit excellent wide-angle performance, maintaining single-point focusing up to a 30° incidence angle with an electric field enhancement exceeding 15 dB. The proposed millimeter-wave transparent metasurface features a simple structure, supports wide-angle incidence, and can be deployed over large areas with adjustable focal points to meet communication requirements. This work provides a reliable solution for mitigating millimeter-wave transmission loss through low-emissivity glass.

1. INTRODUCTION

Recently, the millimeter-wave band, characterized by abundant spectrum resources, low latency, high reliability, and precise beamforming, is a key enabler for ultra-fast wireless networks and a smarter society. Nevertheless, its practical deployment is challenged by high free-space path loss and limited coverage. Meanwhile, advances in metamaterials have positioned metasurfaces as a powerful tool for beam manipulation, making them a promising solution for enhancing signal coverage in hot pot areas [1, 2]. Due to the excessive insertion loss, it is difficult to design metasurfaces directly on walls. Consequently, researchers have turned their attention to transparent glass [3].

To maintain optical transparency, metasurfaces typically employ glass substrates and can be categorized into two main types: one based on patterning ITO films on the glass, and the other on etching metal mesh structures [4–10]. However, both types of metasurfaces are designed on the exterior of the glass. While they can enhance the signal transmission through the glass, their prolonged outdoor exposure makes them susceptible to corrosion, wear, and mechanical damage [11–17]. Additionally, the signal enhancement provided by current metasurfaces remains limited. There have been few studies on using the low-emissivity glass from building structures as a metasurface substrate. Although the unique low-emissivity silver film layer between the glass exhibits strong reflection and low transmission characteristics for millimeter-wave signals, which obstructs indoor coverage, it can be directly utilized for metasurface design. This approach not only avoids wear issues associated with traditional optically transparent metasurfaces but also enhances the millimeter-wave signal transmission capability. Moreover, the low-emissivity coating itself has good optical transparency, and designing a gradient metasurface on it has minimal impact on the overall transparency of the glass.

This paper presents a signal transmission solution that integrates low-emissivity glass with metasurface technology. For signals of different polarization states, the embedded film layers within the low-emissivity glass are utilized to design metasurface structures, leading to the proposal of two distinct design methodologies. The characteristics of the metasurface unit in the millimeter-wave band are analyzed using CST software. By applying the Huygens-Fresnel principle and a gradient phase modulation mechanism, a metasurface array is designed. Under vertical incidence, both metasurfaces achieve an electric field enhancement exceeding 22 dB compared to uncoated glass, while maintaining good wide-angle performance. Simulation results demonstrate that the designed metasurfaces can effectively transmit and focus millimeter-wave signals, thereby enhancing outdoor-to-indoor communication links and offering a new device solution for indoor millimeter-wave coverage.

2. DESIGN OF OPTICALLY TRANSPARENT METASURFACE UNITS

Due to the large distance between the base station and the receiver, the far-field condition of the base station antenna is fully satisfied, and the received signal can be treated as a plane wave. The signal is then focused in the near field by the metasurface, as shown in Fig. 1. This focusing process can be regarded as the reverse of how a lens antenna converts spherical waves into plane waves during transmission. To achieve this, the transmission phase of the phase-gradient metasurface unit must cover a full 2π range [18–25]. Reference [8] investigated the transmis-

* Corresponding author: Jingchang Nan (nanjingchang@lntu.edu.cn).

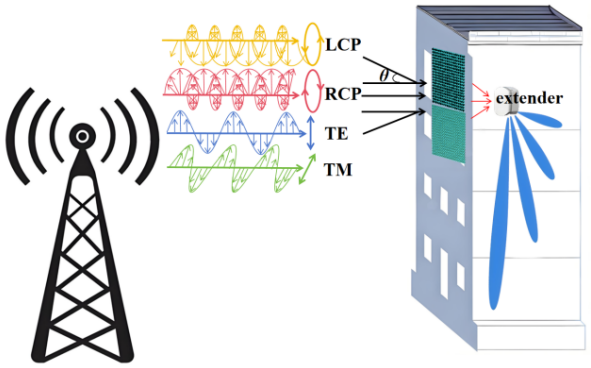

FIGURE 1. Application scenario schematic.

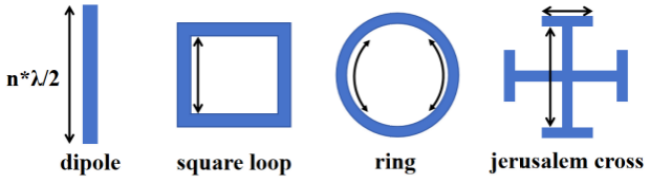

FIGURE 2. Common unit forms.

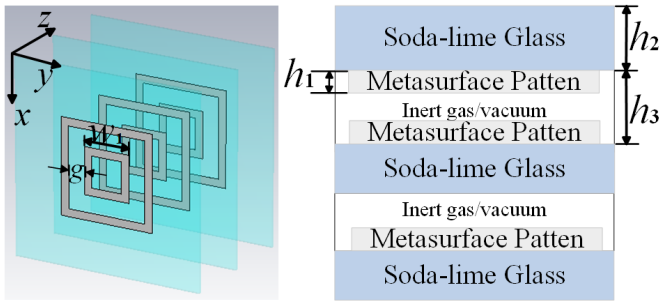

FIGURE 3. Triple layer metasurface unit structure diagram.

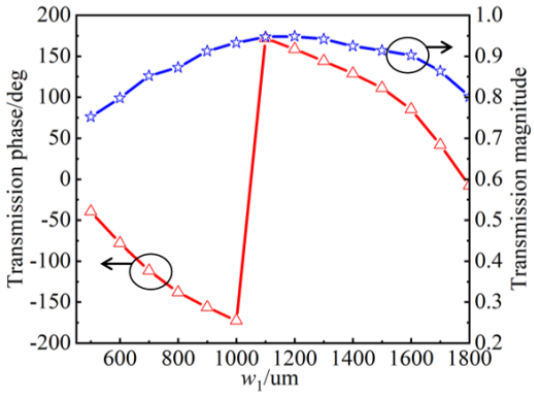

FIGURE 4. The simulated amplitude and phase response when the size of the square ring changes.

sion phase limit of the transmission metasurface. It concluded that to achieve a full 2π transmission phase range while keeping the transmission loss within 3 dB, at least three layers are required for linearly polarized waves, whereas only two layers are needed for circularly polarized waves.

2.1. Design of Three-layer Metasurface Unit

For transmissive metasurfaces, the transmission amplitude and phase of the unit cell are two critical parameters. A key challenge in their design is to create units on a low-emissivity glass substrate that allow for high-efficiency transmission of incident signals while also providing a full 360° phase coverage. Common unit cell geometries include strip dipoles, square rings, circular rings, and Jerusalem crosses, as shown in Fig. 2.

In a strip dipole structure, the dipole length must be an integer multiple of half the wavelength. Upon signal incidence, the dipole resonates and re-radiates energy. For square-ring and circular-ring units, the perimeter of each half-ring must be an integer multiple of half the wavelength. Conceptually, each half-ring acts as a dipole, making the total ring perimeter an integer multiple of the full wavelength. The Jerusalem cross structure operates on a similar resonance principle. This work employs a square-ring-based design. To maximize the transmission phase range, the structure is evolved into a double-square-ring configuration. The transmission phase is tuned by adjusting the unit's geometric dimensions, and the square ring size can be initially estimated using Equation (1):

$$w_1 = n * \lambda/4 \tag{1}$$

The transmission phase tuning is achieved by adjusting the dimensions of the multi-layer metasurface units. Within the 3 dB transmission loss range, the transmission phase can cover a full 360°. Based on the structural characteristics of low-emissivity glass, a metasurface unit is proposed as shown in Fig. 3. The unit is a multilayer stack (from bottom to top): soda-lime glass – silver film – soda-lime glass – silver film – silver film – soda-lime glass. The parameters related to soda-lime glass and silver film are sourced from low-emissivity glass manufacturers. The thickness of the silver film h_1 is 2 µm, with a sheet resistance of 0.1 Ω/sq. The thickness of the soda-lime glass h_2 is 100 µm, with a dielectric constant of 7. The gap between the glass layers h_3 is 2530 µm. The design employs a double-square-ring configuration to exploit dual-resonance characteristics. The unit period is 7500 µm, and the gap between the inner and outer square rings g is fixed at 1300 µm. The transmission phase variation of the unit is controlled by adjusting the edge length w_1 of the square rings. The width of the inner square ring ranges from 500 to 1800 µm.

The structure is simulated in CST with periodic boundary conditions (unit cell) applied in the x and y directions, and an open boundary condition with additional space in the z direction. A linearly polarized plane wave propagates along the z-axis, illuminating the periodically arranged unit cells in the x-y

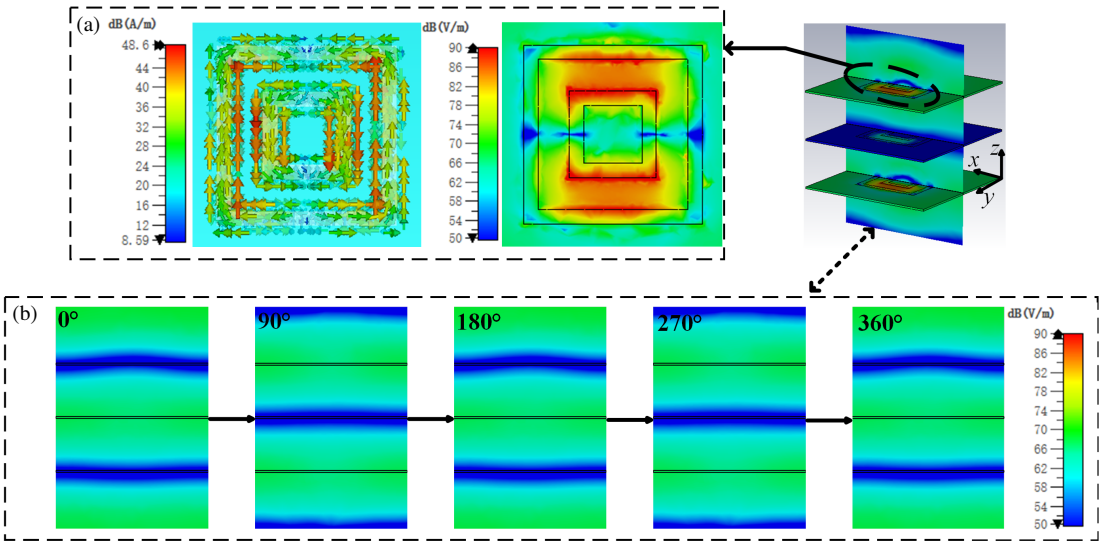

FIGURE 5. Simulation results of metasurface elements. (a) Induced current distribution. (b) Side field distribution.

plane. At the center frequency of 28 GHz, Fig. 4 shows the variation of transmission phase and amplitude as functions of the square ring edge length. The unit structure is able to ensure that the transmission phase reaches 2π within the transmission loss range of less than 3 dB.

Taking the response of the unit at the center frequency of 28 GHz with a plane wave signal as an example, the distribution of the surface induced current and the side field distribution of the unit are examined. Fig. 5(a) shows the distribution of induced current around the square ring in the frequency-domain simulation, indicating that the unit structure can effectively resonate. The side field distribution of the unit at five different phase moments are shown in Fig. 5(b). The metasurface unit structure facilitates coupling between the layers of the low-emissivity glass, enabling effective energy transfer and thereby ensuring efficient signal transmission.

2.2. Design of a Double-layer Metasurface Unit

For circularly polarized signals, various approaches can provide full phase coverage. Herein, we employ the element rotation method, grounded in polarization transformation theory, using a two-layer open-ring structure. This unit achieves a full 2π transmission phase range while maintaining an insertion loss below 3 dB. Consider a right-handed circularly polarized (RCP) plane wave incident on the unit along the $-z$ direction. Its electric field can be expressed as:

$$E_i = E_0(x + jy)e^{jk_0z}e^{jwt} \tag{2}$$

An incident RCP plane wave can be decomposed into two orthogonal, linear polarization components. The transmission responses of the unit to these two components are denoted as T_x and T_y, respectively. Assuming an ideal lossless condition, the transmission amplitude for both components is unity. Under this assumption, the transmission coefficients are given by Equation (3):

$$T_x = 1 \cdot e^{j\varphi_x} \quad T_y = 1 \cdot e^{j\varphi_y} \tag{3}$$

where φ_x and φ_y are the transmission phases for the two orthogonal components, respectively, the transmitted field is consequently given by Equation (4):

$$E_t = E_0\left(xe^{j\varphi_x} + jye^{j\varphi - y}\right)e^{jk_0z}e^{jwt} \tag{4}$$

When a phase difference of π exists between the two components, the expression in Equation (4) reduces to Equation (5):

$$E_t = E_0(x - jy)e^{j\varphi_x}e^{jk_0z}e^{jwt} \tag{5}$$

Equation (5) demonstrates that the incident RCP wave is fully converted to a co-propagating LCP wave, with the transmitted wave acquiring a phase shift of φ_x. When the unit is rotated counterclockwise by an angle θ, the transmitted field, derived through a process analogous to that leading to Equation (5), is given by Equation (6):

$$E_t = E_0(x - jy)e^{j2\theta}e^{j\varphi_x}e^{jk_0z}e^{jwt} \tag{6}$$

A comparison of Equations (5) and (6) reveals that a counterclockwise rotation of the unit by an angle θ advances the transmission phase by 2θ (not 2 degrees), while the transmission coefficient remains unchanged. Consequently, rotating the unit from 0° to 180° provides a full 360° phase coverage, maintaining stable and high transmission efficiency throughout. Analogously, for an incident LCP wave, the same rotation introduces a phase delay of 2θ in the transmitted field, which is efficiently converted to RCP. The configuration of the dual-layer metasurface unit is depicted in Fig. 6. Its key geometric parameters are as follows: the interlayer thickness h_3 is 1890 μm; the metasurface silver film thickness h_1 is 2 μm; the outer ring radius R is 2014 μm; the inner ring radius r is 1621 μm; and the opening length L is 970 μm.

Figure 7 presents the transmission phase and amplitude versus the rotation angle, confirming that the unit achieves a full 2π phase shift. The induced current and field distributions under signal incidence are shown in Fig. 8, which clearly indicate effective structural resonance and energy coupling via the open ring. Furthermore, the side-view field distributions at five representative phase points reveal the energy propagation mecha-

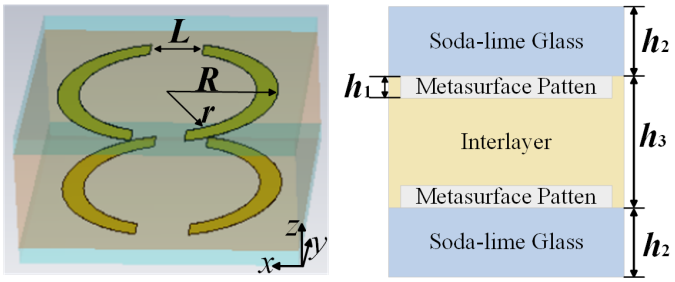

FIGURE 6. Double layer metasurface unit structure diagram.

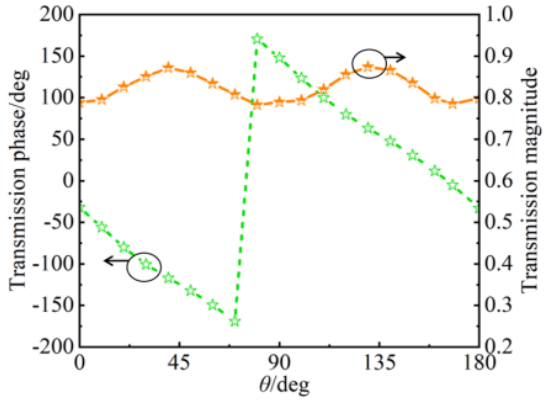

FIGURE 7. The transmission phase and amplitude corresponding to different rotation angles.

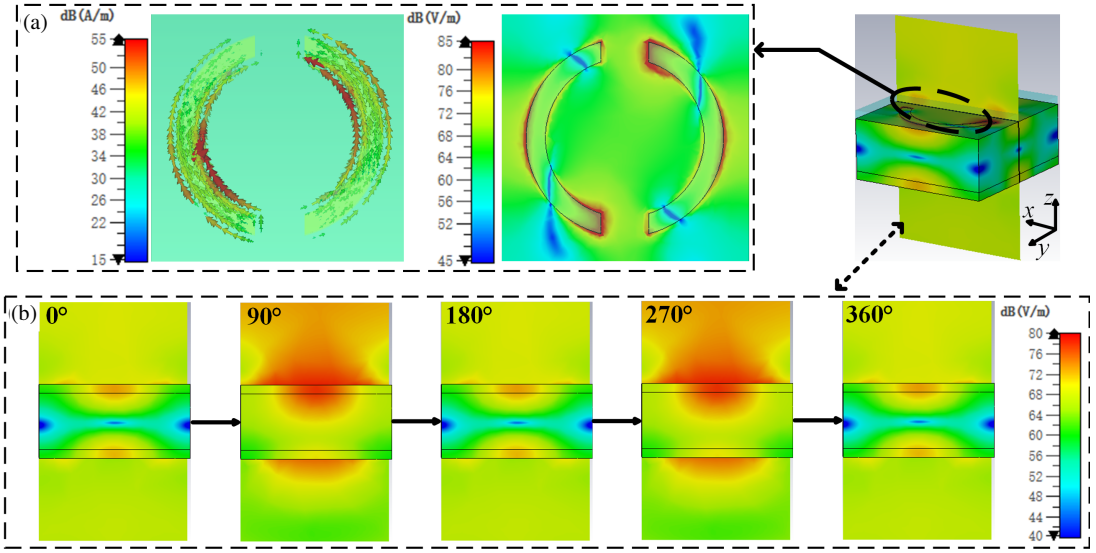

FIGURE 8. Simulation results of metasurface elements. (a) Induced current distribution. (b) Side field distribution.

nism: energy couples into the interlayer through the upper open ring, propagates in a waveguide mode, and is finally received and re-radiated by the lower open ring.

3. DESIGN AND RESULTS ANALYSIS OF PHASE GRADIENT METASURFACE ARRAY

The lens of the antenna converts the spherical wave of the antenna into a plane wave and emits it, thus enabling the inverse design of the metasurface, so that the far-field plane wave emitted by the base station is focused at a preset position. Based on the Huygens-Fresnel principle and the gradient phase modulation mechanism, the metasurface pattern is designed. When a plane wave is incident, the metasurface imposes a spatially varying phase profile, which introduces controlled phase advances or delays across the wavefront [26].

A spatial gradient in the transmission phase introduces a progressive shift of the wavefront, which steers the entire beam toward the region of phase delay. Consequently, to achieve focusing, the phase profile $\varphi(x, y)$ across the metasurface array must conform to the following condition in Equation (7):

$$\varphi(x, y) = \frac{2\pi\left(\sqrt{F^2 + R^2} - F\right)}{\lambda}, \tag{7}$$

where $\varphi(x, y)$ is the phase difference required for focusing, λ is the wavelength at the center frequency, F is the target focal length and R is the distance from each unit on the metasurface array to the focal point.

3.1. Three-layer Square Ring Metasurface Array

The focal length of the metasurface is set to 3 cm, with a center frequency of 28 GHz, corresponding to a wavelength of 11.11 mm. The phase difference of the metasurface units is calculated using Equation (7), and the unit size is determined based on the relationship between the phase difference and the square ring size. The metasurface array consists of 20×20 units, with a planar size of 15 cm $\times$ 15 cm. The metasurface units are strictly center-symmetric square ring structures. Based on the phase gradient modulation mechanism, it is known that the phase dif-

Phase distribution/deg

									4.6
								24.6	-161
							49	-139	44
						78	-111	71	-97
					116	-77	103	-65	136
				166	-33	145	-24	177	26
			-124	27	-160.5	28	-131.5	78.3	-65
		-23	112.2	-85	98	-64	145	1.8	-135
	133	-121	24	-164	27	-128	87	-51	177
15.6	76	-173	-22.7	154.5	-9.6	-160.5	58	-77	153

w_1/um

									1770
								1730	915
							1690	802	1695
						1610	685	1642	640
					1472	595	1535	565	1357
				1145	1900	1297	1857	1070	1727
			740	1725	915	1726	755	1625	565
		1853	1495	605	1565	565	1297	1775	780
	1375	727	1733	945	1725	750	1595	545	1070
1750	1627	1000	1853	1225	1805	915	1665	595	1235

FIGURE 9. Transmission phase distribution of 1/8 metasurface.

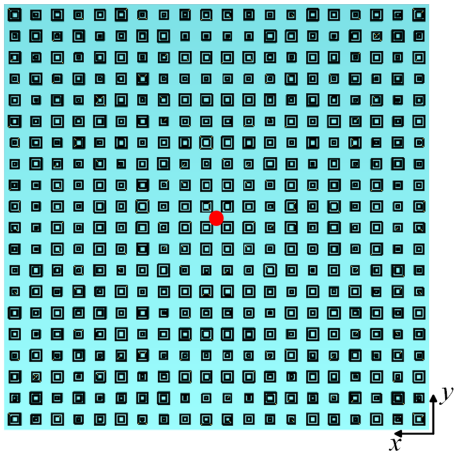

FIGURE 10. Metasurface pattern.

ference distribution of the array also exhibits symmetry. Therefore, only 1/8 of the metasurface structure's phase difference distribution needs to be calculated, and a mirror operation is used to obtain the entire metasurface array structure. The relationship between the phase difference distribution of each unit and the square ring size w_1 is shown in Fig. 9.

The model of the entire phase-gradient metasurface is shown in Fig. 10. The arrangement achieves a continuous phase gradient across the aperture, which is essential for effective wavefront manipulation and focusing.

The metasurface is simulated in CST, with the z-direction being the signal incident and exit direction. The boundary conditions are set as open (add space), and the boundaries in the other directions are also set to open. The incident angle of the plane wave is sequentially adjusted to 0°, 15°, and 30°, in order to observe the wide-angle performance of the metasurface. The simulation results are shown in Fig. 11. It can be seen that the energy is concentrated at the preset central spot. When the incident angle is 30°, the focal point displacement radius is controlled within 2.1 cm, demonstrating good wide-angle performance. The designed metasurface exhibits excellent signal enhancement effects.

The three-layer blank glass without metasurface film layer was simulated in CST, and the glass thickness, dielectric constant and observation position were consistent with the metasurface. Compared to the blank glass, the simulation results are further quantified, and the enhanced electric field intensity at the focal point is shown in Fig. 12. In the range of 26–30 GHz, the metasurface can effectively enhance the electric field intensity of the signal. When the incident angle is vertical, the electric field enhancement can reach 23.98 dB. Fig. 12 demonstrates that the metasurface has good wide-angle performance. Even at a 30° oblique incidence, compared to vertical incidence, the enhancement effect has decreased by 5 dB. This might be due to the fact that there is still room for improvement in the angular sensitivity of the square ring-shaped element. Adopting a strictly center-symmetric structure should bring about an improvement. Although the enhancement effect has declined, it is still above 15 dB, exhibiting excellent millimeter-wave signal enhancement.

3.2. Dual-layer Open-ring Metasurface Array

The design method of the phase gradient metasurface allows for the free adjustment of the array's size and focal distance during the design phase according to communication requirements. To distinguish it from the three-layer metasurface array, the focal length of the dual-layer metasurface array is set to 5 cm, and the center frequency of the metasurface is set to 27 GHz. The phase difference of the metasurface unit is calculated using Equation (7). The circular ring structure with an opening introduces additional phase differences through different rotation angles, enabling the unit to rotate from 0° to 180° and achieve complete 360° phase coverage. Because the dual-layer open-ring metasurface tunes the phase difference by adjusting the rotation angle, a corresponding relationship between the phase difference and the unit rotation angle can be obtained. The metasurface array is composed of 20×20 units, with a planar size of $10.148\,\text{cm} \times 10.148\,\text{cm}$. The corresponding relationship between the phase difference and the rotation angle for the 1/8 metasurface structure is shown in Fig. 13. The entire structure is obtained by mirror rotation, as shown in Fig. 14.

Simulation was performed in CST with incident angles of 0°, 15°, and 30°, where the incident wave is a right-hand circularly polarized plane wave, to observe the signal enhancement performance of the metasurface. The results of the plane wave in-

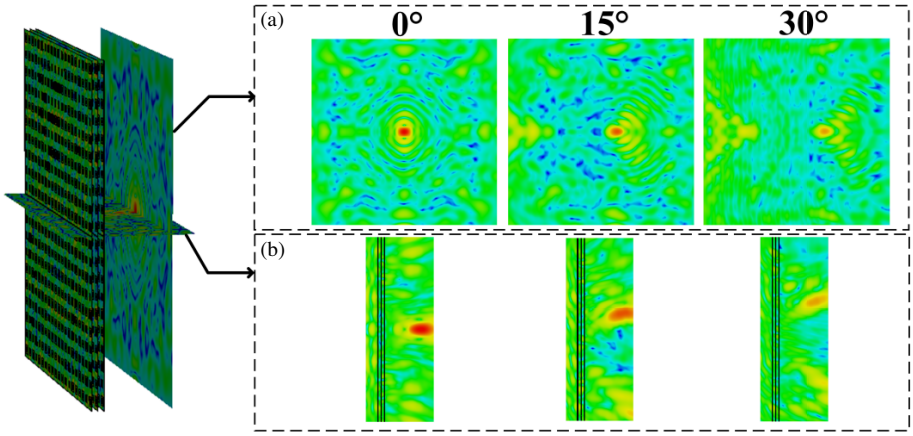

FIGURE 11. Simulation results of electric field distribution. (a) The field distribution of the focal plane. (b) Side field distribution.

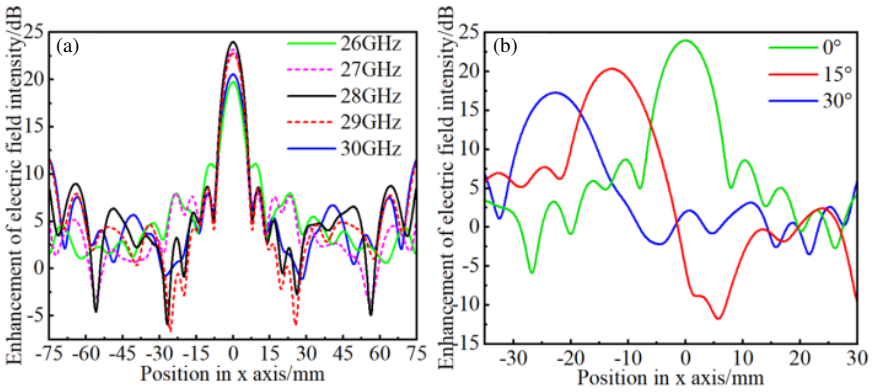

FIGURE 12. Enhancement of electric field intensity. (a) X-axis. (b) Incident angle.

Phase distribution/deg

									18
								-162	-70
							26	113.5	-152
						-136	-53	37	135
					76	151	-124	-30	70
				-58	10	88	176	-88	15
			-171	-113	-43.5	37	126	-135.5	-30
		99	145	-157	-85	-3	87	-171	-65
	36	68	114	174	-113	-30	63	164	-88
0	20	52	99	160	-128	-44	50	151	-100

Rotation angle/deg

									156
								67	16
							152	104	61
						52	9	146	95
					122	88	45	0	126
				11	161	116	77	24	158
			71	38	5	146	99	52	0
		110	91	64	22	167	116	71	14
	146	127	104	78	38	0	130	82	24
165	155	137	110	85	48	5	138	88	30

FIGURE 13. Transmission phase distribution of 1/8 metasurface.

cident at different angles are shown in Fig. 15. From the figure, it can be observed that after the signal incident, the metasurface effectively focuses the signal, and the focal point shift distance for a 30° oblique incidence is controlled within 3.2 cm.

Double-layer blank glass without metasurface film was simulated and set up in CST, with the glass thickness, dielectric constant and observation position remaining consistent with the metasurface. The results are compared with the blank glass without the metasurface pattern. The electric field strength enhancement of the metasurface is shown in Fig. 16, and the results varying with the incident angle are shown in Fig. 16. The results indicate that the dual-layer circular ring metasurface array can effectively enhance the intensity of circularly polarized millimeter-wave signals.

4. COMPARISON OF DIFFERENT DESIGNS

Table 1 presents a comparison between this work and other recent related studies. Compared to other metasurfaces, this work integrates the metasurface between low-radiation glass layers,

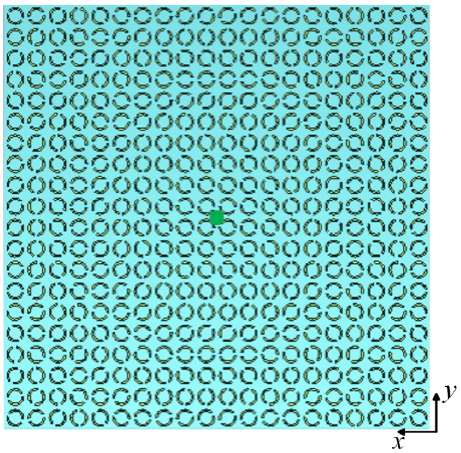

FIGURE 14. Metasurface pattern.

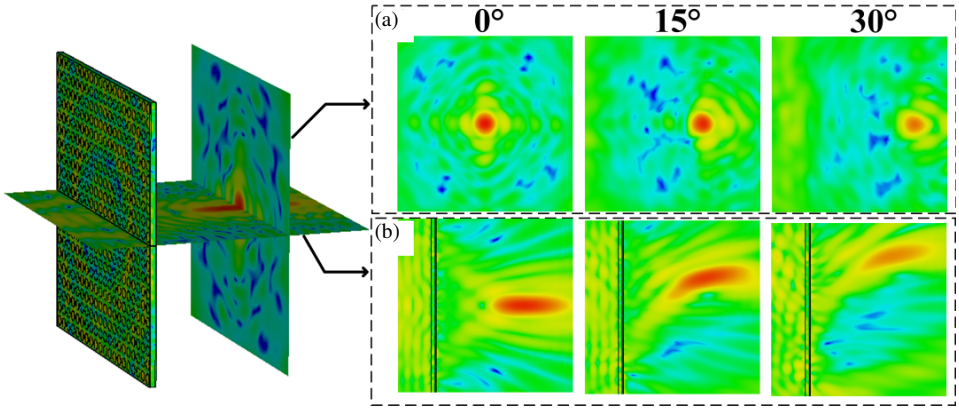

FIGURE 15. Simulation results of electric field distribution. (a) The field distribution of the focal plane. (b) Side field distribution.

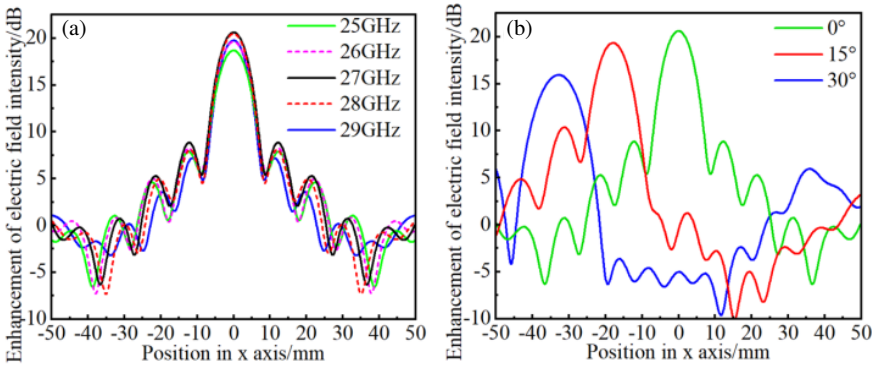

FIGURE 16. Enhancement of electric field intensity. (a) X-axis. (b) Incident angle.

TABLE 1. Comparison of different designs.

Reference	Material	Incident angle	Polarization type	Enhancement (dB)	Low-E process
[1]	metal mesh	$\pm 45^\circ$	LP	-	No
[3]	Cu	-	-	10	No
[4]	ITO	0°	LP	-	No
[5]	Ag metal mesh	$\pm 20^\circ$	LP	5	No
[6]	Silver	$\pm 20^\circ$	LP	5	No
This work	Low-E silver film	$\pm 30^\circ$	LP, CP	> 22	Yes

offering better stability and enhanced electric field intensity. The metasurface we designed is more aligned with practical applications, avoiding the issue of wear and failure when metasurfaces are placed on the exterior of glass. Most importantly, this work is the first to propose designing a low-radiation film-layer metasurface between low-radiation glass layers, which supports wide-angle incidence and meets the communication needs of millimeter-wave signals from outdoor to indoor.

5. CONCLUSION

This paper innovatively utilizes the film layer between low-radiation glass to design the metasurface. Based on different signal polarization forms, two unit structures are proposed, and the characteristics of these unit structures are analyzed to explain the working principle of the metasurface array. The operating frequency bands of the two metasurfaces are 26.3–29.8 GHz and 25.5–29 GHz, respectively. Compared to blank glass, the enhancement of the electric field intensity can be increased to 23.98 dB and 22.12 dB, with the maximum incident angle reaching 30°. The metasurfaces enhance both linearly and circularly polarized signals. In the future, base stations, metasurfaces and indoor repeaters can form a new type of millimeter-wave indoor communication coverage system, providing a novel solution to address the challenges of millimeter-wave communication blockage.

ACKNOWLEDGEMENT

I would like to thank the National Natural Science Foundation of China (61971210), my supervisor, Prof. Nan Jingchang, and Liaoning Key Laboratory of Radio Frequency and Big Data for Intelligent Applications for providing the necessary financial support for my research.

REFERENCES

[1] Wei, Z., H. Xue, Y. Li, S. Zhao, Z. Chen, and L. Li, "A hybrid RF and solar integrated energy harvesting system using optically transparent metasurface," *IEEE Transactions on Antennas and Propagation*, Vol. 73, No. 2, 920–927, 2025.

[2] Cai, Y., P. Mei, X. Q. Lin, and S. Zhang, "Efficient beam manipulation with phase symmetry operations on transmitarrays for flat-top beams," *IEEE Transactions on Antennas and Propagation*, Vol. 72, No. 10, 7536–7545, 2024.

[3] Kim, B., S. Bang, S. Kim, D. Kwon, S. Kim, and J. Oh, "Locally optimal periods in periodic optically transparent two-metal-layered refractive metasurfaces for outdoor-to-indoor communication," *IEEE Antennas and Wireless Propagation Letters*, Vol. 24, No. 5, 1253–1257, 2025.

[4] Li, L., P. Zhang, F. Cheng, M. Chang, and T. J. Cui, "An optically transparent near-field focusing metasurface," *IEEE Transactions on Microwave Theory and Techniques*, Vol. 69, No. 4, 2015–2027, 2021.

[5] Jiang, R. Z., Q. Ma, J. C. Liang, Q. Y. Zhou, J. Y. Dai, Q. Cheng, and T. J. Cui, "A single-layered wideband and wide-angle transparent metasurface for enhancing the EM-wave transmissions through glass," *IEEE Transactions on Antennas and Propagation*, Vol. 71, No. 8, 6593–6605, 2023.

[6] Hong, S., Y. Kim, and J. Oh, "Automobile laminated glass window embedded transmitarray and ray tracing validation for enhanced 5G connectivity," *IEEE Transactions on Antennas and Propagation*, Vol. 70, No. 8, 6671–6682, 2022.

[7] Liu, G., M. R. D. Kodnoeih, K. T. Pham, E. M. Cruz, D. González-Ovejero, and R. Sauleau, "A millimeter-wave multibeam transparent transmitarray antenna at Ka-band," *IEEE Antennas and Wireless Propagation Letters*, Vol. 18, No. 4, 631–635, 2019.

[8] Abdelrahman, A. H., A. Z. Elsherbeni, and F. Yang, "Transmission phase limit of multilayer frequency-selective surfaces for transmitarray designs," *IEEE Transactions on Antennas and Propagation*, Vol. 62, No. 2, 690–697, 2014.

[9] Zhang, X., F. Yang, S. Xu, A. Aziz, and M. Li, "Dual-layer transmitarray antenna with high transmission efficiency," *IEEE Transactions on Antennas and Propagation*, Vol. 68, No. 8, 6003–6012, 2020.

[10] Liu, G., H.-J. Wang, J.-S. Jiang, F. Xue, and M. Yi, "A high-efficiency transmitarray antenna using double split ring slot elements," *IEEE Antennas and Wireless Propagation Letters*, Vol. 14, 1415–1418, 2015.

[11] Feng, P.-Y., S.-W. Qu, and S. Yang, "Octave bandwidth transmitarrays with a flat gain," *IEEE Transactions on Antennas and Propagation*, Vol. 66, No. 10, 5231–5238, 2018.

[12] Dai, X., G.-B. Wu, and K.-M. Luk, "A wideband circularly polarized transmitarray antenna for millimeter-wave applications," *IEEE Transactions on Antennas and Propagation*, Vol. 71, No. 2, 1889–1894, 2023.

[13] Kitayama, D., Y. Hama, K. Goto, K. Miyachi, T. Motegi, and O. Kagaya, "Transparent dynamic metasurface for a visually unaffected reconfigurable intelligent surface: Controlling transmission/reflection and making a window into an RF lens," *Optics Express*, Vol. 29, No. 18, 29 292–29 307, 2021.

[14] Kitayama, D., A. Pander, Y. Hama, and H. Takahashi, "Alignment-free twisted-split-ring metasurface on single substrate with 2π phase range for linearly polarized sub-terahertz wave," *Optics Express*, Vol. 31, No. 13, 20 769–20 786, 2023.

[15] Wang, S., P. C. Wu, V.-C. Su, Y.-C. Lai, C. H. Chu, J.-W. Chen, S.-H. Lu, J. Chen, B. Xu, C.-H. Kuan, *et al.*, "Broadband achromatic optical metasurface devices," *Nature Communications*, Vol. 8, No. 1, 187, 2017.

[16] Soghi, S., H. Heidar, M. R. Haraty, and V. Nayyeri, "Single-layer broadband optically transparent metamaterial absorber using gold thin film," *IEEE Transactions on Microwave Theory and Techniques*, Vol. 72, No. 6, 3743–3752, 2024.

[17] Nguyen, M. A. and G. Byun, "Anisotropic metagratings with a polarization selective layer for anomalous wide-angle reflection and polarization conversion," *IEEE Transactions on Antennas and Propagation*, Vol. 72, No. 10, 7961–7969, 2024.

[18] Cai, X., Z. Chu, F. Wu, X. Fu, H. Sun, Y. Han, J. Yang, R. Zhu, T. Liu, and J. Wang, "Metasurface window with customized transparency for sunlight and switchable transmission for microwaves," *IEEE Transactions on Microwave Theory and Techniques*, Vol. 73, No. 7, 3670–3682, 2025.

[19] Kim, B. and J. Oh, "Single-glass-layer optically transparent transmitarray with high aperture efficiency and low profile at 5G millimeter-wave band," *IEEE Transactions on Antennas and Propagation*, Vol. 71, No. 11, 9036–9041, 2023.

[20] Safari, M., Y. He, M. Kim, N. P. Kherani, and G. V. Eleftheriades, "Optically and radio frequency (RF) transparent metaglass," *Nanophotonics*, Vol. 9, No. 12, 3889–3898, 2020.

[21] Safari, M., N. P. Kherani, and G. V. Eleftheriades, "Multifunctional metasurface: Visibly and RF transparent, NIR control and low thermal emissivity," *Advanced Optical Materials*, Vol. 9, No. 17, 2100176, 2021.

[22] Huang, J., T.-K. Wu, and S.-W. Lee, "Tri-band frequency selective surface with circular ring elements," *IEEE Transactions on Antennas and Propagation*, Vol. 42, No. 2, 166–175, 1994.

[23] Zhang, F., X. Cheng, and Y. Yao, "A passive transparent metasurface based on low-emissivity glass," in *2024 International Conference on Microwave and Millimeter Wave Technology (ICMMT)*, 1–3, Bejing, China, 2024.

[24] Li, J., A. Jana, Y. Yuan, K. Zhang, S. N. Burokur, and P. Genevet, "Exploiting hidden singularity on the surface of the poincar sphere," *Nature Communications*, Vol. 16, No. 1, 5953, 2025.

[25] Yuan, Y., W. Zhou, R. Wang, Y. Wang, Y. Dong, S. N. Burokur, and K. Zhang, "Non-orthogonal metasurfaces for channel-locked spin-orbital transitions," *Advanced Photonics*, Vol. 7, No. 5, 056009, 2025.

[26] Li, H., Y.-Q. Pang, B.-Y. Qu, J.-S. Zheng, and Z. Xu, "Optical transparent metasurface lenses and their wireless communication efficiency enhancement," *Acta Physica Sinica*, Vol. 73, No. 14, 144104, 2024.